Electronic Supplementary Material (ESI) for Dalton Transactions.

Supporting Information

Slow magnetic relaxation in a $\{Co^{II}Co^{III}_2\}$ complex containing a high magnetic anisotropy trigonal bipyramidal Co^{II} centre

Alexandra Collet,[a] Gavin A. Craig,[‡a] María José Heras Ojea,[§a] Lakshmi Bhaskaran,[b] Claire Wilson,[a] Stephen Hill[b] and Mark Murrie[a]

[a] *WestCHEM, School of Chemistry, University of Glasgow, University Avenue, Glasgow, G12 8QQ, UK. E-mail: mark.murrie@glasgow.ac.uk*

[b] *Department of Physics and NHMFL, Florida State University, Tallahassee, USA*

‡ Current address: Institute for Integrated Cell-Material Science (WPI-iCeMS), Kyoto University, Yoshida, Sakyo-ku, Kyoto 606-8501, Japan

§ Current address: School of Chemistry, The University of Manchester, Manchester M13 9PL, U.K.

Contents **Page**

1. Experimental section and physical measurements

$[Co^{II}Co^{III}_2(\mu_3\text{-OH})(\mu\text{-pz})_4(DBM)_3]\cdot 2MeCN$ (**1**·2MeCN)

$CoCl_2.6H_2O$ (0.1 mmol, 24 mg) was added to a solution of Hpz (0.3 mmol, 20 mg) and HDBM (0.3 mmol, 67 mg) in 16 ml MeOH/MeCN (1:1) in the presence of NEt_3 (2 mmol, 0.3 ml). The solution was stirred for 1 hour at room temperature, and left to slowly evaporate to give red block-like crystals after 4 days (~15% yield). Selected IR peaks (cm^{-1}): 3495 (w), 3060 (w, br), 2253 (w), 1595 (s), 1373 (s), 1301 (m), 1219 (m), 1178 (m). Elemental analysis calcd(%) for **1** $C_{57}H_{46}Co_3N_8O_7$: C 60.49%, H 4.10%, N 9.90%, found C 60.12%, H 4.09%, N 9.73%.

Complex **1**·2MeCN is a new solvate of the complex $[Co^{II}Co^{III}_2(\mu_3\text{-OH})(\mu\text{-pz})_4(DBM)_3]\cdot 2THF$. [1]

Single-Crystal X-ray Diffraction: Crystallographic data were collected at 100 K using Mo – K_α radiation (λ = 0.71073 Å) using a Nonius Kappa CCD diffractometer with an Oxford Cryosystems cryostream low temperature device.

Powder X-Ray Diffraction (PXRD): PXRD measurements were carried out at 298 K using a PANalytical X'Pert PRO diffractometer (λ (CuKα) = 1.4505 Å) on a mounted bracket sample stage over the range of $5° < 2\vartheta < 30°$ using a step size of 0.0334°.

Magnetic Susceptibility Measurements: Variable-temperature direct current (DC) and alternating current (AC) magnetic susceptibility data were collected on a Quantum Design MPMS-XL SQUID magnetometer equipped with a 5 T magnet operating in the 290 - 2 K range. Polycrystalline samples were embedded in eicosane, to prevent torquing. Magnetic data have been corrected for diamagnetism (Pascal's constants and corrections for the sample holder).

Microanalysis: Elemental analyses (C, H, and N) were performed in-house in the School of Chemistry at the University of Glasgow.

High-field EPR: High-field/frequency EPR spectra were collected on a microcrystalline powder sample of **1**, which was immobilized in a polyethylene cup with a Teflon® stopper. The transmission-type spectrometer used in this study employed a 17 T superconducting magnet.[2] Microwave frequencies were generated in the 48 to 615 GHz range using a phase-locked Virginia Diodes source combined with a series of frequency multipliers. The field modulated EPR signal, *dI*/*dB* (where *I* represents the absorption intensity and *B* the magnetic field strength), was obtained via lock-in detection using an InSb hot-electron bolometer (QMC Ltd., Cardiff, U.K.). Variable temperature measurements were performed in the range from 2 to 20 K using an Oxford Instruments (Oxford, U.K.) continuous-flow cryostat.

2. Powder X-Ray Diffraction analysis

The experimental powder X-ray diffraction (PXRD) pattern of the complex is shown in Figure S1. It is clear that there is a deviation from the pattern calculated from the single crystal structure and this could be attributed to the loss of solvent, during the grinding process, as seen in the elemental analysis. In order to examine if the desolvation is the reason for the deviation of the experimental pattern from the calculated pattern, the sample was prepared in a different way, by avoiding grinding the sample to powder. The new PXRD pattern (Figure S2) is now closer to the calculated one, which suggests that desolvation causes the deviation seen in Figure S1. This

desolvation could cause a slight change of the crystal packing and therefore a slight change of the local environment around the cobalt centres, resulting in small changes to the *g*, *D* and *E* parameters.
The difference in the intensities of the peaks could also be attributed to the desolvation, while the slight shift in 2ϑ values of the peaks is due to the temperature difference between the experimental PXRD pattern, measured at room temperature, while the calculated pattern is generated from the single-crystal data collected at 100 K.

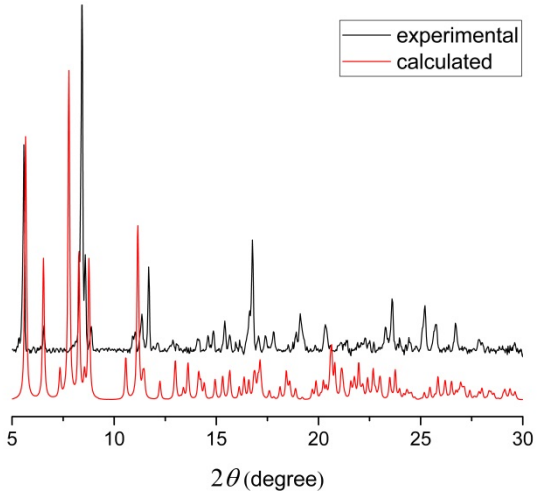

Figure S1. The powder X-ray diffraction pattern of the desolvated complex (ground). The red line represents the calculated powder X-ray diffraction pattern for the solvated complex **1**·2MeCN and the black line the experimental one. The experimental PXRD pattern was measured at room temperature, while the calculated pattern is generated from the single-crystal data collected at 100 K.

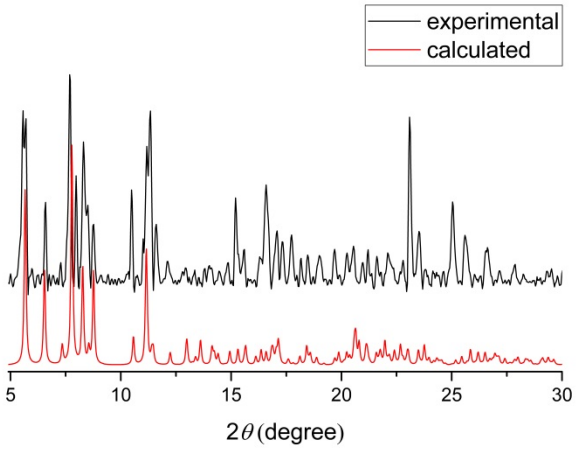

Figure S2. The powder X-ray diffraction pattern of the solvated complex (not ground). The red line represents the calculated powder X-ray diffraction pattern for the solvated complex **1**·2MeCN and the black line the experimental one. The experimental PXRD pattern was measured at room temperature, while the calculated pattern is generated from the single-crystal data collected at 100 K.

3. Single-Crystal X-ray Diffraction

The crystal showed signs of being split. The two components are related by a rotation of 4.9 degrees about reciprocal axis 0.837 0.463 1.000 and real axis 1.000 0.320 0.615 and are related by the following twin law: 0.997 0.029 -0.011 / -0.061 1.006 0.048/ 0.037 -0.050 0.993.
The data were integrated as a two component twin and the file for a single component from this processing was ultimately used as it gave the best results.
Data collection: *COLLECT*; cell refinement: *SAINT* v8.34A; [3] data reduction: *SAINT* v8.34A; [3] program used to solve structure: ShelXT; [4] program used to refine structure: *SHELXL*; [4] molecular graphics: Olex2; [5] software used to prepare material for publication: Olex2. [5]

Table S1. Data collection and crystallographic parameters for compound **1**·2MeCN.

Chemical formula	$C_{57}H_{46}Co_3N_8O_7 \cdot 2(C_2H_3N)$
M_r	1213.91
Crystal system, space group	Triclinic, *P*-1
Temperature (K)	100
***a*, *b*, *c* (Å)**	13.25 (1), 14.173 (11), 16.426 (13)
α, β, γ (°)	85.880 (19), 71.750 (19), 72.444 (18)
***V* (Å^3)**	2792 (4)
Z	2
Radiation type	Mo *K*α, λ = 0.71073 Å
μ (mm^{-1})	0.95
Crystal size (mm)	0.34 × 0.1 × 0.06
Diffractometer	KappaCCD
T_{min}, T_{max}	0.79, 1.00
No. of measured, independent and observed [$I > 2\sigma(I)$] reflections	15656, 9616, 6683
R_{int}	0.043
$R[F^2 > 2\sigma(F^2)]$, $wR(F^2)$, S	0.047, 0.111, 1.06
No. of reflections	9616
No. of parameters	736
No. of restraints	1
H-atom treatment	H atoms treated by a mixture of independent and constrained refinement
Δ>max, Δ>min (e Å^{-3})	0.59, −0.50
Absorption correction: multi-scan TWINABS-2012/1 (Bruker,2012) was used for absorption correction.	

Table S2. The CShMs values calculated with the program SHAPE [6] for each geometry for the five-coordinate Co1.

Geometry	Value
Pentagon	35.9
Vacant octahedron	7.1
Trigonal bipyramid	**0.33**
Spherical square pyramid	5.55
Johnson trigonal bipyramid	2.35

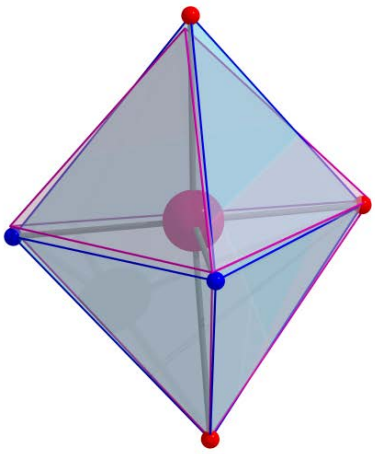

Figure S3. The closest reference polyhedron for TBP geometry calculated with SHAPE [6] (pink polyhedron) and the polyhedron formed by the Co1 centre and the peripheral ligands (blue polyhedron). Colour code: Co^{II}: dark pink, O: red, N: blue, bonds: grey.

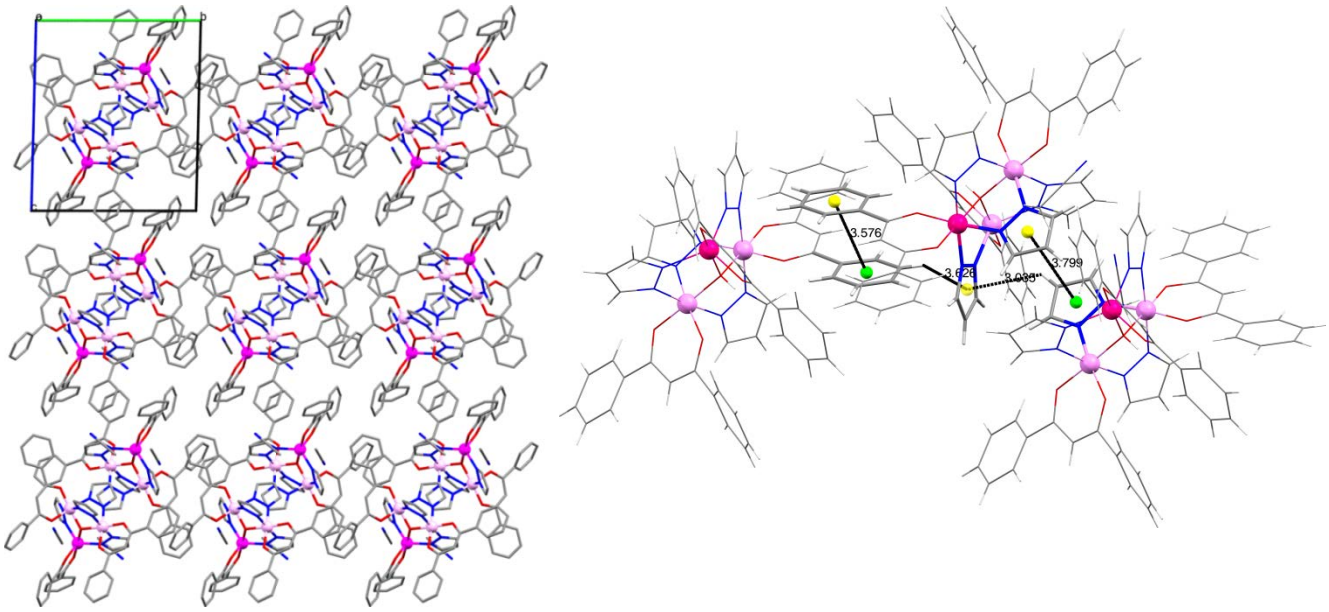

Figure S4. *Left:* The crystal packing of **1**·2MeCN. Colour code: Co^{II}: dark pink, Co^{III}: light pink, O: red, N: blue, C: grey. Hydrogen atoms are omitted for clarity. *Right:* Illustration of the hydrogen-π and π-π intermolecular interactions. The yellow spheres (central molecule) and the green spheres (side molecules) represent the centroids of the phenyl and pyrazolate rings. The dashed black lines show the distances between the centroids and between the hydrogens and the centroids. Colour code: Co^{II}: dark pink, Co^{III}: light pink, O: red, N: blue, C: grey, H: white.

4. High-field EPR analysis

A representative series of temperature-dependent EPR spectra recorded at a frequency of 203.2 GHz are displayed in Figure S5. Spectral features are clearly visible at all temperatures that are clustered into three groups, which we have labeled g_x^{eff}, g_y^{eff} and g_z^{eff}, representing the three components of the effective Landé-tensor associated with the lowest-lying Kramers doublet of the $s = 3/2$ ground state manifold. All of the features exhibit the same temperature dependence, i.e., they increase uniformly in intensity with decreasing temperature, confirming their assignment as ground state-transitions. Within each cluster, one can clearly resolve two distinct resonances of more-or-less equal intensity, suggesting the presence of discrete species within the powdered sample, having distinct spin-Hamiltonian parameters; a weaker signal is also discernible in between the two main g_y^{eff} resonances. It is apparent that one of the resonances within each pair is sharper than the other. Assuming that the observation of multiple resonances is due to a distribution of microenvironments, then the distribution width should be a unique fingerprint for each set of resonances. Hence, the resonance linewidths provide a means of distinguishing the two microenvironments. We have thus labeled the sharper resonances with open symbols and the broader ones with closed symbols (see also Figure S5). The associate g^{eff} values are then obtained from fits to resonance positions deduced at multiple frequencies, as shown in Figure S5: (sharp) $g_x^{eff} = 5.11(2)$, $g_y^{eff} = 3.51(3)$ and $g_z^{eff} = 1.98(1)$; (broad) $g_x^{eff} = 5.47(2)$, $g_y^{eff} = 3.27(1)$ and $g_z^{eff} = 1.91(1)$. As can be seen, the species with the sharper distribution is less rhombic whilst the species with the broader distribution is more rhombic.

Although it is not possible to constrain the zero-field splitting parameters *D* and *E* on the basis of EPR transitions associated with the lowest Kramers doublet, it is possible to constrain the sign of *D*. The observation of two g^{eff} values well above 2.00, and one near or below 2.00, is indicative of an easy-plane type anisotropy (positive *D* value for the $s = 3/2$ ground state). Moreover, both species are appreciably rhombic. In fact, one can deduce values for the *E*/*D* ratio and the real *g*-tensor components associated with the $s = 3/2$ spin state from the following perturbative expressions:

$$g_x^{\text{eff}} = g_x\left(1+\frac{1+3\gamma}{\sqrt{1+3\gamma^2}}\right);\ g_y^{\text{eff}} = g_y\left(1+\frac{1-3\gamma}{\sqrt{1+3\gamma^2}}\right);\ g_z^{\text{eff}} = g_z\left(\frac{2}{\sqrt{1+3\gamma^2}}-1\right), \quad (E1)$$

where $\gamma = E/D$. If we then make the assumption/approximation that $g_x = g_y$ (due to over-parameterization), we obtain the following parameters for the two species: (sharp) $E/D = 0.13$, $g_{xy} = 2.18$ and $g_z = 2.07$; (broad) $E/D = 0.17$, $g_{xy} = 2.23$ and $g_z = 2.08$.

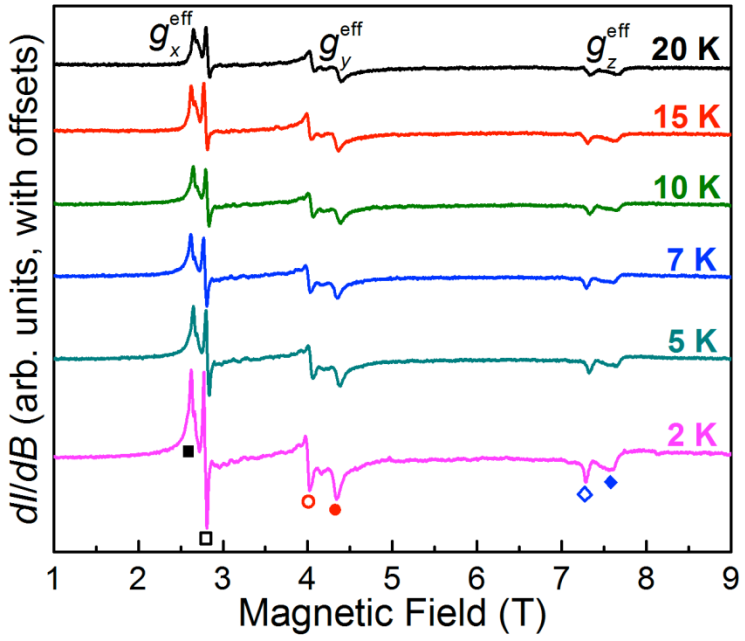

Figure S5. Variable temperature EPR spectra recorded at a frequency of 203.2 GHz. Each cluster of peaks has been labelled at the top of the figure according to the corresponding component of the effective *g*-tensor associated with the lowest Kramers doublet. Within each cluster, the two resonances have been labelled with open and closed symbols according to the same scheme as in Figure S5 (see text for further explanation).

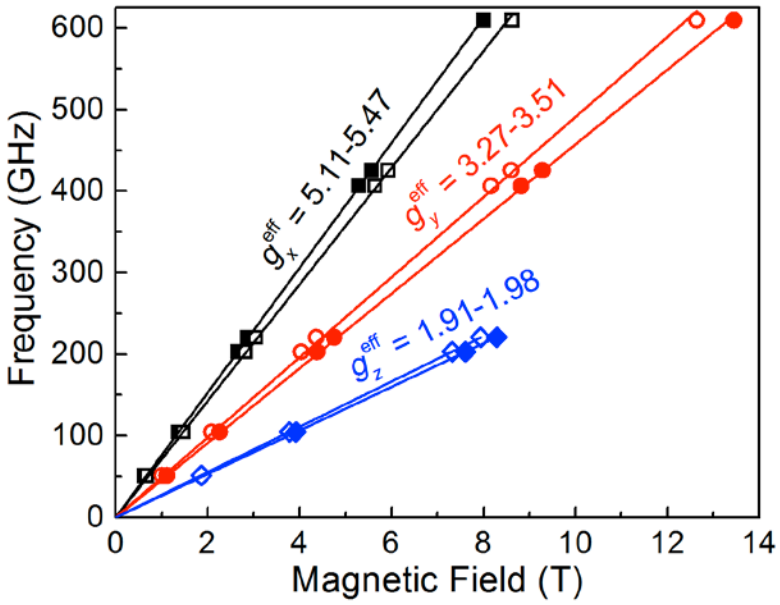

Figure S6. Frequency versus field plot of the resonance positions obtained from multi-frequency measurements. Effective *g*-values are deduced from linear fits (solid lines) to each data set, which are labelled by open and closed symbols of different shape/colour (see text and Figure S5 for further explanation).

5. Ac magnetic susceptibility

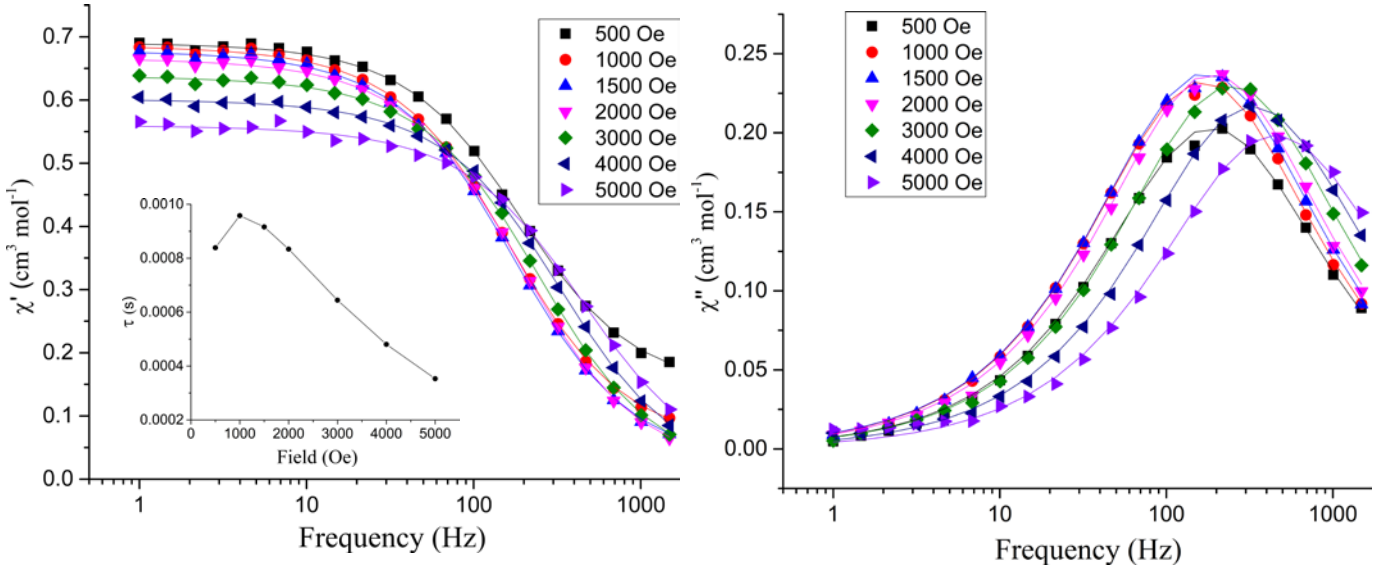

Figure S7. Frequency dependent in-phase (left) and out-of-phase (right) AC susceptibility signals for complex **1** under different applied DC fields at 2 K. The solid lines correspond to the fit (CC-FIT programme) [7] *Inset (left):* Plot of τ values versus the applied DC fields (the solid line is a guide to the eye).

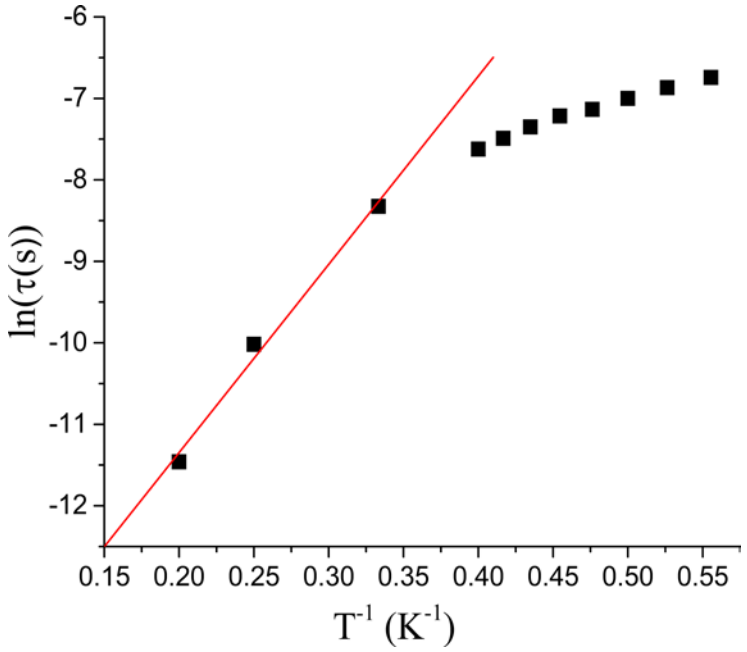

Figure S8. Arrhenius plot of $\ln(\tau)$ data versus T^{-1} of **1** at 1000 Oe in the temperature range of 1.8 – 5 K. The solid red line represents the fit only with Orbach process ($\ln\tau = \ln(\tau_0) + \frac{\Delta E}{k_B T}$) at higher temperatures.

6. References

1. M. Lukasiewicz, Z. Ciunik, J. Mazurek, J. Sobczak, A. Staron, S. Wołowiec and J. J. Ziołkowski, *Eur. J. Inorg. Chem*., 2001, 1575.
2. A. K. Hassan, L. A. Pardi, J. Krzystek, A. Sienkiewicz, P. Goy, M. Rohrer and L. C. Brunel, *J. Magn. Reson.,* 2000, **142**, 300.
3. SAINT v8.34a, © 1997 - 2013, Bruker AXS Inc., Madison, WI.
4. G. M. Sheldrick, *Acta Crystallographica C*, 2015, **C71**, 3.
5. O. V. Dolomanov, L. J. Bourhis, R. J. Gildea, J. A. K. Howard and H. Puschmann, *J. Appl. Cryst.*, 2009, **42**, 339.
6. S. Alvarez, M. Llunell, *J. Chem. Soc., Dalton Trans.*, 2000, 3288; M. Llunell, D. Casanova, J. Cirera, P. Alemany and S. Alvarez, Shape Program, Version 2.0, 2010.
7. CC-FIT Copyright © 2014 N. F. Chilton; Y.-N. Guo, G.-F. Xu, Y. Guo and J. Tang, *Dalton Trans*., 2011, **40**, 9953.